New Journal of Physics
The open-access journal for physics

Real-time observation of transient electron density in water irradiated with tailored femtosecond laser pulses

C Sarpe, J Köhler, T Winkler, M Wollenhaupt and T Baumert[1]
Universität Kassel, Institut für Physik und CINSaT, Heinrich-Plett-Strasse 40, D-34132 Kassel, Germany
E-mail: tbaumert@physik.uni-kassel.de

New Journal of Physics **14** (2012) 075021 (16pp)
Received 6 March 2012
Published 24 July 2012
Online at http://www.njp.org/
doi:10.1088/1367-2630/14/7/075021

Abstract. Ionization mechanisms in water irradiated with bandwidth-limited and temporally asymmetric femtosecond laser pulses are investigated via ultrafast spectral interferometry. By using a novel common-path interferometer with an enlarged temporal measurement window, we directly observe the dynamics of free-electron plasma generated by shaped pulses. We found that a temporally asymmetric pulse and its time-reversed counterpart address multiphoton and avalanche ionization mechanisms in a different fashion. Positive third-order dispersion shaped pulses produce a much higher free-electron density than negative ones at the same fluence, instantaneous frequency and focusing conditions. From the experimental data obtained after irradiation with bandwidth-limited and shaped pulses the multiphoton and avalanche coefficients were determined using a generic rate equation. We conclude that temporal tailored femtosecond pulses are suitable for manipulation of the initial steps in laser processing of high band gap materials.

[1] Author to whom any correspondence should be addressed.

Contents

1. Introduction

The interaction of intense ultrashort laser pulses with transparent dielectrics has attracted much attention in the last decade due to its applications in precise micro- and nano-processing (see, for example, [1, 2] and references therein) or medical surgery [3, 4]. These materials are transparent for light in the visible and near infrared spectral region but they become highly absorptive if laser pulses of sufficient intensity are used. On this basis, high-intensity ultrashort laser pulses are a unique tool in processing and structuring transparent dielectrics. For these materials the first step in the ablation process is optical breakdown in which a high density of free electrons is generated through nonlinear ionization processes. The free electrons absorb energy from the laser pulse, transfer it to the ions, atoms and molecules, and on a longer timescale ablation takes place. The quality of the ablation process is strongly dependent on the primary processes involved in the laser–matter interaction. Even if it is well known that the free electrons are generated through multiphoton, avalanche or tunneling ionization [5–8], the contribution of each ionization mechanism for different materials and laser pulse parameters is not completely understood. Englert *et al* [9] showed that by using temporally asymmetric shaped femtosecond laser pulses created via applying third-order dispersion (TOD) in a Fourier transform pulseshaper the basic ionization mechanisms can be controlled in the case of solid transparent dielectrics. In that case, TOD-tailored laser pulses showed different thresholds for ablation for a temporal asymmetric pulse and its time-reversed counterpart. In addition, holes with a diameter one order of magnitude below the optical diffraction limit were produced. Even if the transient electron density generated by shaped pulses was not measured in the above mentioned experiments, a theoretical model based on the interplay of multiphoton and avalanche ionization suggested that the positive TOD pulses, starting with a high intensity sub-pulse followed by a sequence of low intensity sub-pulses create higher free-electron density in comparison to their time-reversed counterpart. The results obtained by numerically solving the multiple rate equations [7] were in qualitatively good agreement with the post mortem ablation analysis for the thresholds of material processing.

In this contribution, we present our studies to investigate in real-time the free-electron density of transient plasma produced by shaped temporally asymmetric ultrashort laser pulses in a thin water jet. Water is an amorphous semiconductor with an energy band gap of 6.5 eV [10].

The study of breakdown dynamics in water is important first of all for micro-processing of biological samples and micro-analytics [4, 11]. In addition, due to the fact that the optical breakdown primary processes are general ones [8], useful information on the behavior of solid dielectrics can also be obtained. Because the laser-induced phenomena are extremely fast, only optical methods can be used to study the dynamics of the free-carriers by probing changes in the optical properties of the laser-excited region. It is generally assumed that material ablation occurs when the concentration of free carriers is on the order of $N_e \sim 10^{21}\,\mathrm{cm}^{-3}$, whereas the real-time experimental measurement of density is still a challenging task. Ultrafast imaging [12–15] and time-resolved reflection microscopy [16] can provide useful information about free-carrier dynamics by measuring the transmission or the reflection coefficient of the electron–hole plasma but these techniques are either not accurate enough or can be used only for laser intensities close to the breakdown threshold. Interferometric techniques can access both the real and imaginary parts of the complex dielectric function and very small changes in the optical properties of free-electron plasma can be detected. Spatial [17, 18] and spectral interferometry [19–22] were successfully used to measure the dynamics of free-electron plasma after irradiation with intense ultrashort laser pulses. In spatial interferometry, thin transparent samples are placed in one arm of a Mach–Zehnder interferometer and are excited by a strong femtosecond pulse. The image is produced by the interfering probe pulse passing through the dielectric sample and the reference one propagating in the other arm of the interferometer. The phase and amplitude obtained by Fourier analysis of the interference picture provide information about the complex dielectric index of the plasma. By changing the time delay between the pump and the pair of reference and probe pulses, complete dynamics can be recorded. In spectral interferometry both the pump and reference pulses, separated by a fixed time delay, propagate through the sample to monitor the changes of the refractive index produced by the pump pulse. The probe and reference pulses (created in a Michelson-type interferometer) are sent to an imaging spectrometer and a frequency–domain interference is produced. If the time delay between the pump and the pair reference–probe pulses (generally the second harmonic of the pump) is adjusted in such a way that the reference pulse propagates through the interaction area before the pump creates the free carriers and the probe after their creation, the phase difference and the contrast of the interference fringes gives direct information about the optical properties of plasma. The advantage of spatial interferometry is its ability to directly monitor the dynamics on a longer timescale but the experimental set-up is more complicated. Spectral interferometry is a simpler and more robust technique, but the time delay between the reference and the probe is generally limited to a few ps even if a high-resolution spectrometer is used to resolve the interference fringes. In order to monitor the dynamics of the free-carrier plasma produced by temporally shaped pulses spread out in time one needs a temporal measurement window broader than the duration of the temporally tailored pulses. In our study, we used an improved spectral interferometer in order to circumvent the above-mentioned disadvantage of the technique.

We make use of a common-path interferometer in which the reference and probe pulses are generated as ordinary and extraordinary beams when the light propagates through birefringent crystals. Our approach was stimulated by van Dijk *et al* [23] where a set-up for single nanoparticles detection is described. The common-path approach leads to a stability much higher than in conventional interferometers. To overcome the problem that a large measurement window would require a high-resolution spectrometer we decreased the delay between interfering pulses again with the help of another birefringent crystal before

analysis. This technique including an enlarged measurement window was hitherto not used in combination with spectral interference. We demonstrate that it is a powerful tool to investigate the dynamics of ultrafast processes on a longer timescale.

The paper is organized as follows. We describe in section 2 the experimental set-up and the principle of spectral interferometry. In section 3, we discuss the optical properties of free-electron plasma relevant to our data evaluation. The experimental results for irradiation with both bandwidth-limited and temporal asymmetrical shaped femtosecond laser pulses are presented in section 4. In section 5, a simple model based on a generic rate equation is used to obtain the multiphoton and avalanche coefficients and to simulate the transient free-electron density for shaped pulses. We conclude the paper with a brief summary.

2. Experimental details

The femtosecond pulses used in this experiment are generated by a Femtolasers Femtopower Pro Ti:sapphire multipass amplifier operating at a central wavelength of 785 nm. At the output of the amplifier the temporal duration of the pulses is 30 fs, the repetition rate is 1 kHz and the maximum energy is 800 μJ per pulse. A schematic representation of the experimental set-up is drawn in figure 1. The beam splitter BS reflects 50% of the incoming laser beam and sends it to a liquid crystal modulator-based pulse shaper (Jenoptik SLM-S640d). The description of the device can be found in [24, 25]. In order to tune the intensity of the pump pulses a stepper motor-controlled achromatic half-wave plate (Bernhard Halle) and a high-contrast polarizer (Codixx colorPol VISIR CW 02) are used. After passing through a dielectric recombination mirror the pump beam is focused onto the surface of the free flowing laminar water jet using a 50 mm focal length lens. The beam transmitted through the beam splitter is first directed to an optical delay line driven by a computer-controlled stepper motor in order to control the time delay between the pulses. Then, the second harmonic is generated in a 200 μm thick β-BBO nonlinear optical crystal. Before passing through the crystal, the polarization direction is rotated by 90° with the help of a $\lambda/2$-wave plate in order to ensure horizontal polarization for the second harmonic pulses before they enter the prism compressor used to pre-compensate the strong positive group delay dispersion of the following optical elements. At the same time, by using the prism compressor, the residual fundamental is completely blocked.

In order to create the reference and probe pulses, a common-path interferometer was designed for this experiment. The 400 nm pulse is impinging at normal incidence on the surface of an α-BBO birefringent crystal. This crystal is oriented in such a way that a light pulse propagating through it is split into an ordinary and an extraordinary pulse with equal intensities, orthogonally polarized at $\pm 45°$ relative to the horizontal. The α-BBO crystal is a negative uniaxial medium. Its two refractive indices at 400 nm are $n_o = 1.6963$ and $n_e = 1.5493$ respectively. The extraordinary pulse precedes the ordinary one by a time delay directly dependent on the crystal length. In comparison to Michelson or Mach–Zehnder interferometers, the common-path interferometer based on birefringent crystals delivers the following advantages: first of all, the probe and reference beams have an inherent spatial overlap and the beam profiles are identical. In addition, the stability of the set-up is dramatically increased as environmental perturbations such as temperature and air pressure fluctuations in the laboratory induce a time drift in the two arms of beam splitter-based interferometers.

The blue pulses are spatially overlapped with the pump beam and propagate in the same way through the sample. The dielectric medium used in this experiment is a thin planar distilled

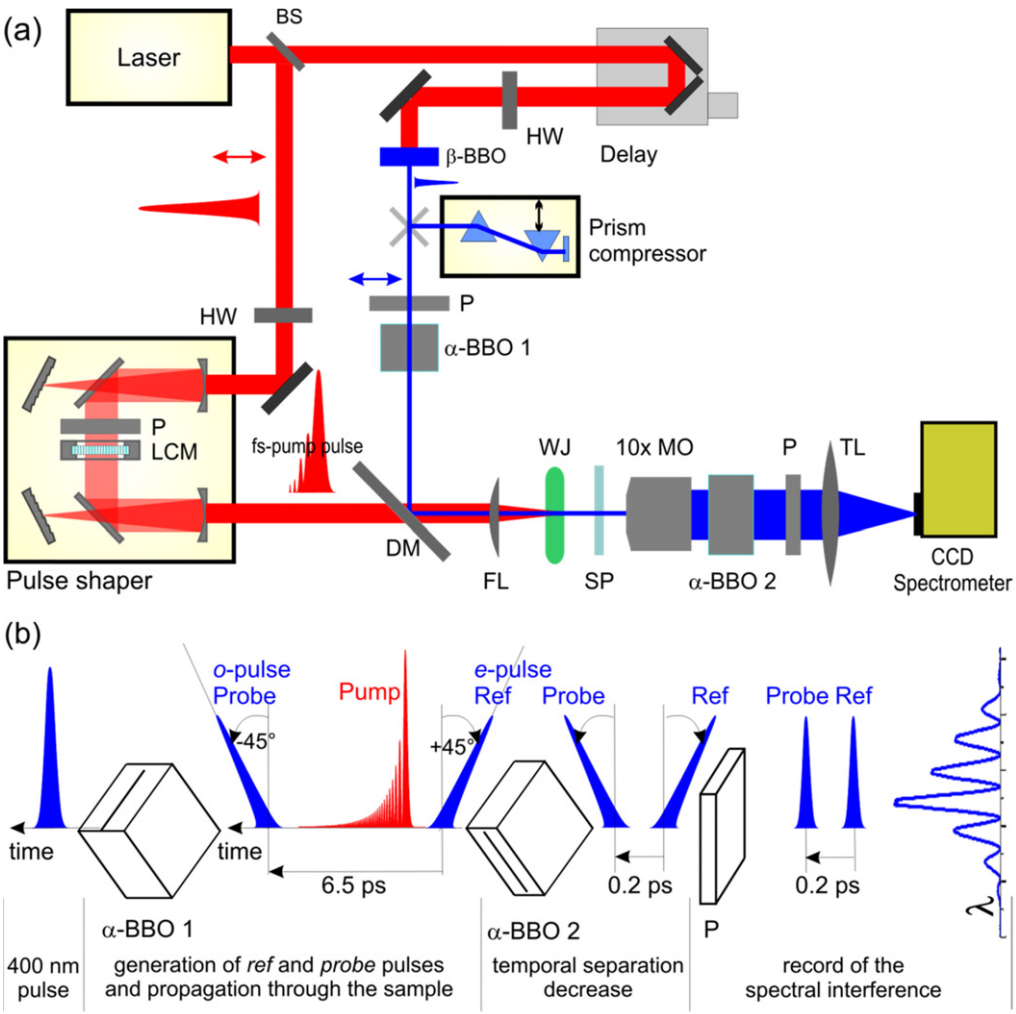

Figure 1. (a) Experimental set-up. Bandwidth-limited or shaped femtosecond laser pulses are focused on the surface of a free flowing planar water jet to generate high-density free-electron plasma. The time sequence and relative polarization for the spectral interference measurements is detailed in (b). A time-delayed pulse is frequency-doubled to 400 nm and passes through a birefringent crystal α-BBO 1. This one creates a pair of orthogonally polarized pulses with a separation of 6.5 ps. The reference and probe pulses propagate through the interaction area together with the pump and probe the changes in the optical properties. A second birefringent crystal α-BBO 2 decreases the temporal separation between the blue pulses to 0.2 ps. After passing through a polarizer the frequency–domain interference pattern is recorded. BS: beam splitter; HW: half-wave plate; P: polarizers; LCM: liquid crystal modulator; DM: dielectric mirror; FL: focusing lens; WJ: free flowing planar water jet; SP: short-pass color filter; MO: microscope objective; TL: tube lens.

water jet produced by a stainless steel nozzle. The thickness of the water jet was measured by spectral interferometry, analyzing the interference fringes of the spectrally broad fundamental beam reflected on the front and respectively the rear water–air interface (set-up not shown in

figure 1). From the inter-fringe separation the thickness of the water jet was found to be 96 μm, smaller than the Rayleigh length of the pump beam in the focus. By using a cutting knife method we have measured a beam waist ($1/e^2$ in the intensity) of the pump beam of 30.5 μm and of the reference/probe pulses of 120 μm. Due to their large diameter and low energy (<5 nJ per pulse) the fluence of the blue pulses is very low and has no effect on the creation of the free electrons. The speed of the water jet was 3 m s^{-1}, assuring a fresh sample area for each laser shot. After passing through the laminar water jet the pump beam is blocked with a short-pass filter and the two blue pulses are used to investigate the optical properties of free-electron plasma. The interaction area is imaged by an infinity corrected microscope objective (Mitutoyo M Plan APO 10x) and a tube lens (400 mm) onto the entrance of a spectrometer fiber. In order to investigate the changes in the refractive index produced only in the center of the pump beam, we used a pinhole in front of the spectrometer fiber [16] to spectrally analyze only the probe and reference beam passing through the maximum free-electron density area. The spectrometer used in this experiment is a Princeton Instruments 320PI fiber optic spectrometer equipped with a 1800 grooves mm^{-1} grating and a cooled CCD array detector. Once dispersed in the spectrometer the pulses having a temporal separation τ produce an interference spectrum (see section 3). The fringes are separated by $2\pi/\tau$ [26] and the position of the maxima and minima is given by the relative phase $\Delta\Phi$ between the pulses, containing information about the electron density. Even if the spectral resolution of the spectrometer used in this experiment is very high, it is not sufficient to fully resolve spectral interference fringes for pulses separated by more than 2 ps.

In order to investigate the effect of shaped laser pulses which cannot be confined in the measurement window or to observe the dynamics on a longer timescale in the relative mode (when both reference and probe pulses propagate after the pump) we changed the set-up of our common-path spectral interferometer: we decreased the temporal separation between the pulses before detection. In order to implement this approach, a second birefringent crystal (α-BBO 2) is used after the infinity corrected objective with the fast axis oriented perpendicularly with respect to the fast axis of the first crystal (see figure 1(b)). In this configuration the first pulse propagates in the second crystal slower than the second one. The reference and probe pulses propagate through the sample separated by $\tau = 6.5$ ps (fixed by the 12.5 mm length of the first birefringent crystal) and the time delay is then decreased to 0.2 ps by passing through the second α-BBO crystal (with a thickness of 12.2 mm). Because the pulses are still orthogonally polarized, a cube polarizer is used to permit interference. The visibility of the fringes is better than 99%. In order to study the dynamics of free–electron plasma, the time delay between the pump and the pair reference–probe is changed by moving the optical delay line. For each time delay the interference spectrum is recorded together with a signal that monitors the energy of the pump pulses.

When the second harmonic pulses propagate through thick birefringent crystals dispersion is introduced (215 fs^2 mm^{-1} for the ordinary beam and 148 fs^2 mm^{-1} for the extraordinary one). As a result different wavelengths of the analyzing pulses pass through the interaction area at different times, decreasing the temporal resolution of the measurement. In order to minimize this effect, we have used the above-mentioned prism compressor to introduce negative group delay dispersion. The adjustment procedure for the temporal duration of the pulses is as follows: by using the prism compressor of the amplifier (not shown) we optimized the second harmonic generation process. In order to have bandwidth-limited pump pulses in the interaction area we adjusted the position of the gratings in the pulse shaper; a temporal duration of 35 fs

was measured with a spectrogram-based method. The prism compressor used for the second harmonic was iteratively adjusted in order to remove the chirp in the probe beam, when all the wavelengths contained in the probe pulse arrive in the interaction area simultaneously with the pump. By optical Kerr effect (OKE) cross-correlation we measured a probe pulse duration of 55 fs.

3. Optical properties of a Drude plasma relevant to data evaluation

The electron densities after laser irradiation are derived from the data assuming homogeneous excitation across the interaction and using the Drude formalism. We measure a phase shift and a change in transmission. Here, we summarize how these quantities can be used to derive electron density for later reference. The optical properties of laser-induced plasma can be described using a generalization of the Lorentz–Drude dielectric function [27]:

$$\varepsilon(\omega) = \varepsilon_{10} - \frac{\omega_{\mathrm{pl}}^2}{\omega^2 + \mathrm{i}\frac{\omega}{\tau_{\mathrm{c}}}}, \tag{1}$$

where ε_{10} describes the contribution of bound electrons, $\omega_{\mathrm{pl}} = e \cdot \sqrt{\frac{N_{\mathrm{e}}}{\varepsilon_0 m_{\mathrm{e}}}}$ is the plasma frequency, τ_{c} is the collision time, ε_0 denotes the vacuum permittivity, m_{e} is the electron mass and e its electric charge. In our experiment, we investigate the dielectric function $\varepsilon(\omega)$ with an ultrashort probe laser pulse around its central frequency ω_0 corresponding to a wavelength of 400 nm. Assuming that the medium is a dielectric one (magnetic permeability $\mu = 1$), the complex refractive index of the Drude plasma is the square root of the dielectric function:

$$\tilde{n}_{\mathrm{Drude}} = \sqrt{\varepsilon(\omega)\mu} \approx \sqrt{\varepsilon(\omega)}. \tag{2}$$

The time-dependent free-electron density $N_{\mathrm{e}}(t)$—on which the plasma frequency is dependent—produces changes in the complex refraction index:

$$\Delta\tilde{n}_{\mathrm{Drude}}(t) = \tilde{n}_{\mathrm{Drude}}(N_{\mathrm{e}}) - \tilde{n}_{\mathrm{Drude}}(N_{\mathrm{e}} = 0) = -\frac{1}{2n_0}\left(\frac{\omega_{\mathrm{pl}}}{\omega}\right)^2 \frac{1}{1 - 1/\mathrm{i}\omega\tau_{\mathrm{c}}}, \tag{3}$$

with $n_0 = \sqrt{\varepsilon_{10}}$ being the linear refractive index of the unperturbed dielectric medium. In addition to the changes produced in the refractive index by the free electrons, in spectral interference methods the contribution of the transient OKE to the refractive index has also to be taken into account:

$$\tilde{n}(t) = n_0 + \Delta\tilde{n}_{\mathrm{Kerr}}(t) + \Delta\tilde{n}_{\mathrm{Drude}}(t). \tag{4}$$

The Kerr effect induces a transient positive contribution to the refractive index, proportional to the pump laser intensity:

$$\Delta\tilde{n}_{\mathrm{Kerr}}(t) = n_2 I(t), \tag{5}$$

where n_2 is the nonlinear refractive index.

In the absolute mode of spectral interferometry (when the reference pulse propagates before the pump and the probe after), the probe pulse only monitors the changes produced by the free carriers: a phase shift due to the changes in the real refractive index and an attenuation produced by plasma absorption. If the electric fields of the reference and probe pulses are: $E_{\mathrm{ref}}(t) = E_0(t)\mathrm{e}^{\mathrm{i}\omega_0 t}$ and $E_{\mathrm{probe}}(t) = \sqrt{T}E_0(t-\tau)\mathrm{e}^{\mathrm{i}[\omega_0(t-\tau)+\Delta\Phi]}$ (where $E_0(t)$ is the envelope,

T is the intensity transmission coefficient and τ the time delay between the blue pulses), the power spectrum is

$$S(\omega) = S_0(\omega)[1 + T + 2\sqrt{T}\cos(\omega\tau - \Delta\Phi)]. \tag{6}$$

The phase shift $\Delta\Phi$ contains information about the real part of the refractive index and the transmission coefficient T about the free-electron plasma absorption. Assuming homogeneous distribution of free-electron density along the sample [18] the phase shift $\Delta\Phi$ and the optical density OD are obtained by taking the real and the imaginary parts of $\Delta\tilde{n}_{\mathrm{Drude}}(t)$:

$$\Delta\Phi = \frac{2\pi}{\lambda} L\,\mathrm{Re}(\Delta\tilde{n}_{\mathrm{Drude}}) = -\frac{\pi L \cdot \omega_{\mathrm{pl}}^2}{\lambda n_0 \left(\omega^2 + \frac{1}{\tau_c^2}\right)}, \tag{7}$$

$$OD = -\frac{4\pi}{\lambda} L \cdot \mathrm{Im}(\Delta\tilde{n}_{\mathrm{Drude}}) = \frac{2\pi L \cdot \omega_{\mathrm{pl}}^2}{\lambda n_0 \omega \tau_c \left(\omega^2 + \frac{1}{\tau_c^2}\right)}. \tag{8}$$

Accordingly, the intensity transmission coefficient T takes the following form:

$$T = \exp(-OD) = \exp\left(-\frac{2\pi L \cdot \omega_{\mathrm{pl}}^2}{\lambda n_0 \omega \tau_c \left(\omega^2 + \frac{1}{\tau_c^2}\right)}\right), \tag{9}$$

where L is the sample thickness and λ is the probe wavelength.

Taking (7), (8) and (1) and assuming a homogeneous electron density across the sample, the free-electron density is directly proportional to the phase shift and the optical density:

$$N_e = \frac{m_e \varepsilon_0}{\pi e^2} \cdot \frac{n_0 \lambda}{L} \cdot \left(\omega^2 + \frac{1}{\tau_c^2}\right) \cdot |\Delta\Phi| = \frac{m_e \varepsilon_0}{2\pi e^2} \cdot \frac{n_0 \lambda}{L} \cdot \tau_c \omega \cdot \left(\omega^2 + \frac{1}{\tau_c^2}\right) \cdot \mathrm{OD}. \tag{10}$$

Equations (7) and (8) contain the collision time τ_c, which can be experimentally derived from the phase shift and transmission measurements according to

$$\tau_c = \frac{2\,|\Delta\Phi|}{\omega OD}. \tag{11}$$

4. Experimental results and discussion

4.1. Bandwidth-limited femtosecond pulses

In figure 2(a), we display the frequency–domain interference spectra for three values of the pump–probe time delay. For negative times both reference and probe pulses pass through the sample before the pump creates free electrons and the spectrum shows the spectral interference of two identical pulses. At 2 ps the pump pulse is confined in the measurement window and the probe pulse monitors the optical properties of free-electron plasma. The free electrons show a metal-like behavior within the irradiated volume resulting in a decrease of the real part of the refractive index thus producing a negative phase shift. For pump–probe delays longer than the measurement window both reference and probe interrogate the sample after pump interaction. This is the relative mode in spectral interference measurements and can be used to observe the dynamics on timescales longer than the measurement window defined by the delay between reference and probe. In this paper, we will concentrate only on the early

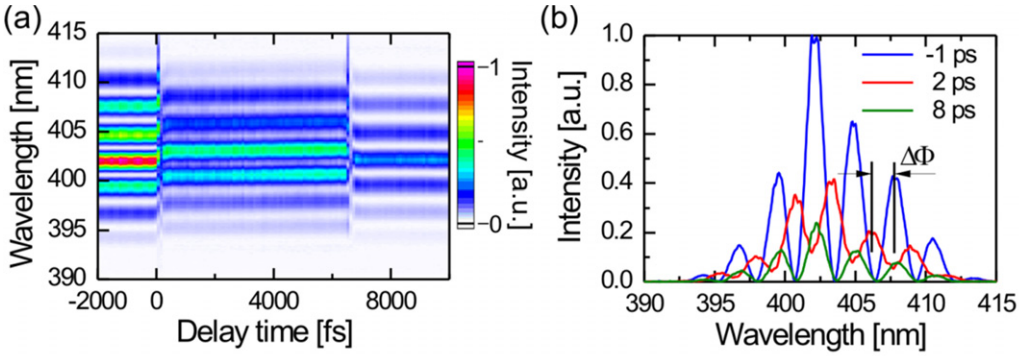

Figure 2. Frequency–domain interference spectra obtained for pump pulse energy of 3.2 μJ. (a) Pseudo-color representation of the spectral interference as a function of the pump–probe time delay. For negative times the pump pulse passes through the sample temporally after the reference and probe. In the measurement window the pump is confined between the two and in the relative mode (after 6.5 ps) the pump propagates before the two blue pulses. (b) Spectra for different time delays. Note the phase shift and the decrease of the fringe visibility introduced by the free-electron plasma.

time dynamics obtained in the absolute mode of spectral interferometry. From the spectral interference data the phase and the transmission coefficient of the probe pulse are calculated by inverse Fourier transformation. The values of the obtained phase shift and transmission coefficient were cross-checked with the values obtained from the shifts of the maxima and minima of the interference fringes. By changing the pump–probe delay the dynamics of the plasma can be constructed. Figure 3 shows the temporal evolution of the phase shift and of the transmission coefficient for a 35 fs bandwidth-limited pulse with respect to different pump pulse energies.

The OKE contribution is proportional to the pump laser intensity (see equation (5)) and it appears only during the pump pulse duration. When the pump and probe pulses overlap (time zero in the figure) there is an increase of the refractive index influencing only the probe pulse and not the reference pulse; this results in an increased optical path between the reference and the probe pulse and a positive shift of the interference fringes is observed. When the pump propagates through the sample simultaneously with the reference pulse, only the latter experiences an increase in the refractive index. However, the optical path between the reference and the probe decreases in this case and an additional negative phase shift (at 6.5 ps in figure 3(a)) appears. When both—Drude and Kerr—contributions are present the interpretation of the measured phase shift and transmission coefficient is ambiguous. In the measurement window there is only a negative phase shift produced by free electrons (equation 7). All our analysis is therefore performed well within the measurement window. For high energies the absolute value of the phase shift decreases in the measurement window and has a small positive value after 6.5 ps (relative mode of spectral interferometry). This is an indication of recombination and further work will be devoted to investigate this effect. For low energies the assumption of homogeneous excitation inside the sample along the propagation direction holds [18, 22] and the phase shift in this case is directly proportional to the electron density. This is the region where we will concentrate our data evaluation and discussion.

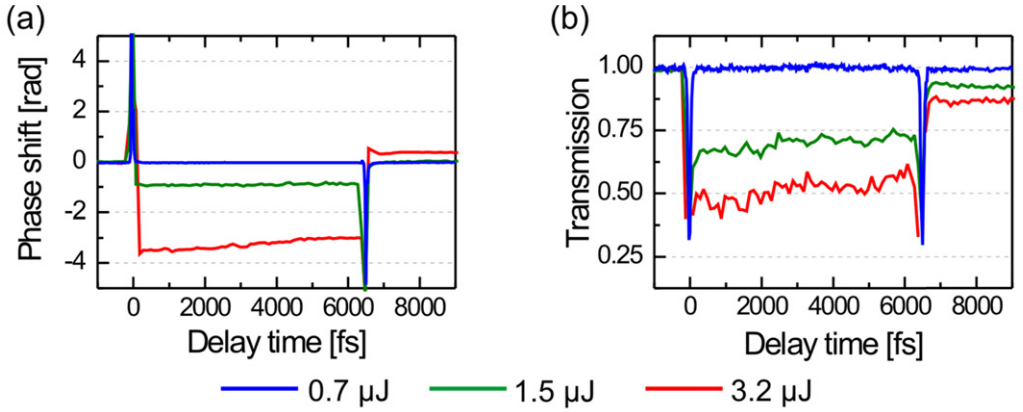

Figure 3. Evolution of phase shift (a) and of probe transmission coefficient T (b) as function of time, after excitation with bandwidth-limited pump pulses (35 fs) for different pump energies. At time zero and at 6.5 ps the pump pulse overlaps with the probe and reference pulses respectively and the phase shift induced by the transient OKE is observed. In the measurement window the negative phase shift and the decrease of the transmission coefficient are due to the generation of free electrons by the pump pulse.

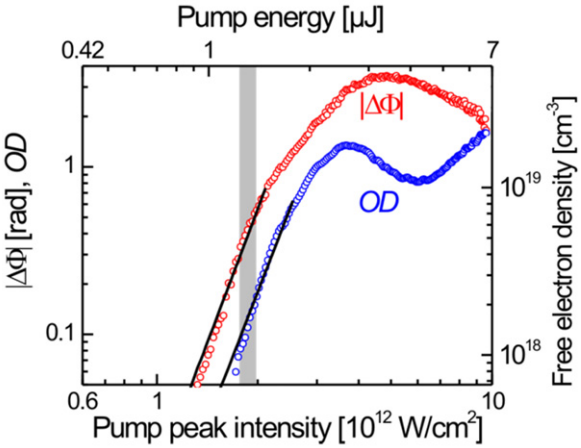

Figure 4. Absolute phase shift $\Delta\Phi$ and optical density OD as a function of the peak pump laser intensity for 35 fs bandwidth-limited pulses together with a fit taking a five-photon ionization process into account (black solid lines). On the right scale the calculated free-electron density assuming a homogeneous distribution (realistic for low laser intensities) is also shown. The light gray window represents the intensity in which an electron collision time of 1.6 ± 0.3 fs was determined.

Figure 4 presents the dependence of the absolute phase shift and of the optical density on the peak pump laser intensity (which is two times higher than the $1/e^2$ averaged intensity) at a time delay of 1.5 ps after the creation of the free electrons. For low intensities the dependence follows a power law indicated by the black lines in figure 4, with an exponent of 5.1 ± 0.2 for the phase shift and 5.2 ± 0.2 for the optical density. This hints at a five-photon

ionization process in the range of 0.1–0.8 rad as also expected from the band gap of 6.5 eV mentioned in the introduction section. By increasing the pump intensity further, the absolute phase shift also increases, but the assumption of a longitudinal homogeneous distribution is not valid anymore and the deviation from the line which indicates the multiphoton process is evident. In this intensity regime a model describing the propagation of light into the dielectric medium [28] will be considered in future investigations. The phase shift reaches a maximum at $4.8 \times 10^{12}\,\mathrm{W\,cm^{-2}}$, for higher intensities it starts to decrease. This behavior was also observed for solid dielectrics [18] and it was attributed to a strong inhomogeneous distribution of free-electron density in longitudinal direction. The visible plasma spark was observed at $9.6 \times 10^{12}\,\mathrm{W\,cm^{-2}}$ peak intensity. Previous studies reported an averaged threshold intensity of $6.6 \times 10^{12}\,\mathrm{W\,cm^{-2}}$ for which the longitudinal distribution of free-electron plasma is on the order of 1 μm [16]. For these values axial distribution acts as a limiting factor in the observed phase shift even if free-electron density is high. A thinner sample provides higher accuracy in the high-intensity excitation regime, whereas a thicker one provides higher resolution for the low-intensity regime. We consider a 100 μm thick sample as a good compromise to study the role of different ionization mechanisms. The optical density is situated below the phase shift but roughly follows the same dependence on pump laser intensity. From the two curves the Drude collision time can be obtained by using equation (11); the value of the collision time was measured to be $\tau_c = 1.6 \pm 0.3$ fs in the intensity range indicated in the figure, where the assumption of a homogeneous distribution is realistic. This value is in good agreement with values presented in the literature from 1.2 fs [16] to 1.7 fs [4].

4.2. Third-order dispersion shaped pulses

We now turn to the topic of control, i.e. how temporally asymmetric laser pulses and their temporal inverted counterparts affect the electron densities when the same fluence is applied. Temporal asymmetric laser pulses were created via Fourier transform pulse shaping applying a third-order spectral phase function (TOD) [29]: $\phi(\omega) = \frac{\phi_3}{3!}(\omega - \omega_0)^3$. The dynamics of the phase shift in the case of TOD-tailored pulses is more complicated when compared to the case of bandwidth-limited ones due to the interplay of transient OKE and the contribution of free electrons. TOD phase shaped pulses consist of trains of pulses (see insets to figure 5 and also figure 7) [30]. In the case of positive TOD the first pulse is the strongest one, followed by weaker pulses whereas in the case of negative TOD the intensity of the sub-pulses in the train increases in time. In figure 5(a), the transient phase shift produced by $+600\,000\,\mathrm{fs}^3$ TOD shaped pulses is presented. By changing the time delay between the pump and the probe pulses, at time zero the first most intense sub-pulse of the train will produce a positive phase shift and eventually free-electron plasma sufficiently dense to be detected.

The absolute value of the negative phase shift produced by the Drude electrons decreases due to the transient OKE produced by the components of the stretched pulse overlapping in time with the probe. The electron density created by such a pulse was analyzed from the transient phase shift at a time delay longer than the temporal distribution of the shaped pulse. In the case of negative TOD shaped pulses, by changing the time delay, the probe will first overlap with the low intensity pulses of the pump, which will generate a positive phase shift in the interference picture. If the intensity is high enough, the strong sub-pulses at the end of the pump will also create detectable free-electron plasma. The arrows in the figures represent the time delays where the final electron density is analyzed for each case. Note that for the same pump pulse energy

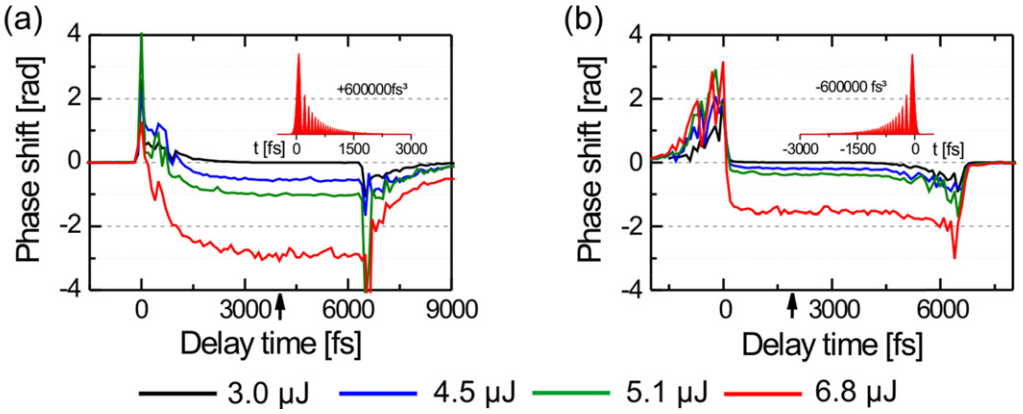

Figure 5. The dynamics of the phase shift for cubic shaped pulses: $+600\,000\,\mathrm{fs}^3$ (a) and $-600\,000\,\mathrm{fs}^3$ (b). The inset in each picture shows the temporal distribution of the laser intensity for the cubic phase applied. Due to the transient OKE the interpretation of the phase shift when the laser pulse overlaps with either reference or probe is ambiguous. The arrows in the figures show the position where the effect of the tailored pulse on the free-electron density is analyzed. Positive shaped pulses produce much higher phase shift than negative pulses with the same energy.

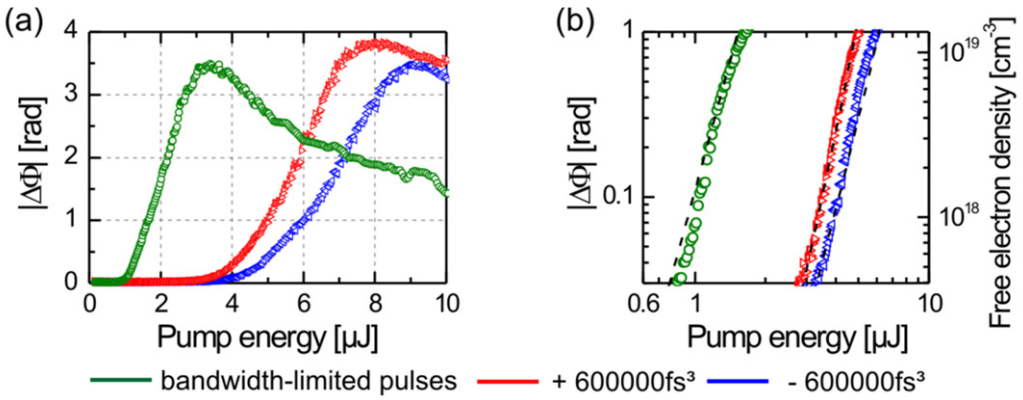

Figure 6. (a) Dependence of the absolute phase shift on the pulse laser energy for bandwidth-limited 35 fs pulses and $+/-600\,000\,\mathrm{fs}^3$ TOD shaped pulses in linear representation. Positive cubic shaped pulses produce a higher phase shift than negative ones for the same total energy. (b) Log–log representation of the phase shift for bandwidth-limited and shaped pulses together with the simulated values (taking both—multiphoton and avalanche ionization—into account) in the range where the homogeneous assumption holds (black dashed lines).

the absolute value of the phase shift produced by positive TOD shaped pulses is higher than the one corresponding to the negative TOD.

In figure 6(a), the dependence of the absolute phase shift on pump laser energy for bandwidth-limited, positive and negative TOD shaped pulses is presented. The threshold values for shaped pulses are higher than for the bandwidth-limited pulse due to the decrease of

maximum laser intensity (of about six times). Note that for the same pump laser energy the spectral interference phase shift produced by the positive shaped pulses is higher than the one produced by negative shaped pulses. At the same time, the maximum phase shift produced by positive cubic shaped pulses is higher than the maximum value produced by negative ones or bandwidth-limited pulses. This is an indication that TOD shaped pulses might be used to optimize the transfer of the laser pulse energy *inside* the transparent dielectric and the topic will be investigated further in the future.

5. Numerical simulations

In order to calculate the dynamics of the plasma produced by shaped pulses we performed a numerical simulation by solving the rate equation for the temporal evolution of free-electron density [31, 32]. For the generation of free electrons, multiphoton and avalanche ionization are considered. Tunnel ionization was neglected for the laser intensities used in this experiment because in the case of bandwidth-limited pulses the power law indicates a multiphoton ionization mechanism (see figure 4) and the effective band gap is considered to be the one of the unperturbed liquid water [10, 32] which requires $k = 5$ photons for ionization. Impact ionization starts, when the electrons reach the critical energy of 1.5 times the effective band gap energy via inverse bremsstrahlung [4]. As inverse bremsstrahlung requires a finite time, Vogel *et al* [4] refined the rate equation model by introducing the retardation $\tau_{\mathrm{ion}} = \tau_{\mathrm{c}} \cdot n$, determined by the mean free time between electron–molecule collisions τ_{c} and the number of photons n to reach the critical energy, in our present study $n = 7$. By considering the retardation, the contribution of the avalanche ionization to free-electron density at time t is determined by the value of the electron density at time $t_{\mathrm{ret}} = t - \tau_{\mathrm{ion}}$. Recombination, diffusion and thermal-ionization are neglected, as these effects do not make a strong contribution to the early time dynamics.

With these assumptions the rate equation is given by

$$\frac{\mathrm{d}N_{\mathrm{e}}(t)}{\mathrm{d}t} = \sigma_k I(t)^k + \alpha \cdot I(t) \cdot N_{\mathrm{e}}(t_{\mathrm{ret}}), \tag{12}$$

where k is the number of photons required for photoionization, σ_k the multiphoton and α is the avalanche coefficient. From our knowledge of the literature there exist no measured values for σ_5 in water and—as remarked by other authors [4]—the photoionization rate calculated by using the Keldysh theory is inappropriate for modeling of optical breakdown in the case of ultrashort laser pulses. It has been shown [4, 18, 33] that for laser pulses with a duration below 40 fs impact ionization makes a small contribution to the generation of free electrons. Based on this assumption we used in the first step the intensity dependence of the phase shift produced by bandwidth-limited 35 fs pulses to fit the multiphoton coefficient for water in a range where the homogeneous excitation assumption holds by taking only multiphoton ionization into account. In the second step we used this value in order to obtain the avalanche coefficient by fitting the spectral interference phase shift produced by positive TOD pulses. As the spectral interference analysis was performed only on a small area in the center of the Gaussian distribution of the pump pulse we used the peak intensities of the pulses and not the spatially averaged values in the fitting procedure. Note that for determination of the coefficients σ_5 and α we use the pulse envelope $E_0(t)$ rather than the rapidly oscillating field $E(t)$. In this way, we obtained the values $\sigma_5 = 0.12 \times 10^{-28}\,\mathrm{s}^{-1}\,\mathrm{cm}^7\,\mathrm{W}^{-5}$ and $\alpha = 14\,\mathrm{cm}^2\,\mathrm{W}^{-1}\,\mathrm{s}^{-1}$. To estimate an error for

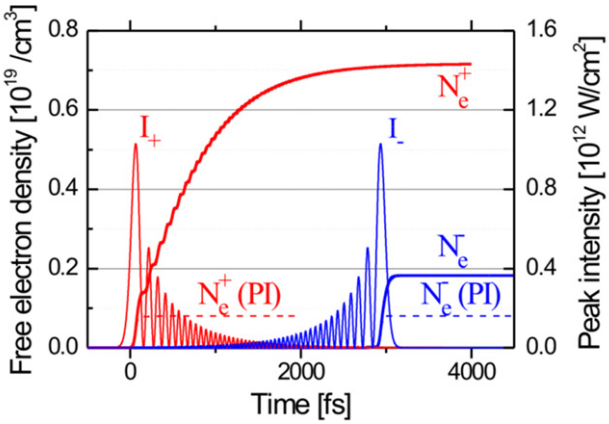

Figure 7. Calculated transient total free-electron density N_e taking multiphoton and avalanche ionization into account (solid lines) for positive (red curves, index +) and negative (blue curves, index −) TOD-modulated pulses. The contribution by pure multiphoton ionization is indicated as well (dashed lines $N_e^+(\mathrm{PI})$, $N_e^-(\mathrm{PI})$). The corresponding transient intensities of the modulated pulses are also presented (I_+, I_-). The curves for negative shaped pulses are offset by 3 ps in time for better visualization. The total energy of the pulses used in simulation is 4.5 μJ.

the coefficients we assume that the measured pump pulse intensity has a maximum error of ±20%. For the +20% limit of intensity the coefficients are: $\sigma_5 = 0.05 \times 10^{-28}\,\mathrm{s^{-1}\,cm^7\,W^{-5}}$ and $\alpha = 12\,\mathrm{cm^2\,W^{-1}\,s^{-1}}$, whereas for the −20% limit $\sigma_5 = 0.38 \times 10^{-28}\,\mathrm{s^{-1}\,cm^7\,W^{-5}}$ and $\alpha = 18\,\mathrm{cm^2\,W^{-1}\,s^{-1}}$ respectively. With the ionization coefficients derived in this way we used the rate equation (12) to obtain free-electron density and the corresponding spectral interference phase shift for bandwidth-limited and shaped pulses. In figure 6(b), the experimental phase shifts and the simulated ones are presented in a log–log representation. The good agreement obtained for negative TOD pulses and the low contribution of the avalanche ionization to free-electron density produced by bandwidth-limited pulses are supporting the validity of the model. At the same time, we have shown that using bandwidth-limited and TOD shaped pulses under the same focusing conditions allows for the determination of both the multiphoton and avalanche ionization coefficients.

In order to study the role of the two ionization mechanisms we simulated the dynamics of free-electron density during the $\phi_3 = \pm 600\,000\,\mathrm{fs}^3$ TOD shaped pulses with the temporal intensity distribution presented in figure 7.

In the same figure (where negative shaped pulses are shifted in time for better visualization), total free-electron density and multiphoton contribution obtained from simulation are presented. For positive cubic phase, electron density increases at the beginning of the pulse due to the effective multiphoton ionization. Later on, the decreasing intensity train of the pulse produces additional free electrons by avalanche ionization. For negative cubic pulses, total free-electron density increases only at the end of the pulse when the free electrons are produced via multiphoton ionization and avalanche. Due to the absence of seed electrons, the low-intensity components in the shaped pulse will not produce free electrons via avalanche ionization. The phase shifts produced by the calculated total free-electron densities for the two cases are 0.57 rad

for the positive shaped pulses and 0.16 rad for the negative one respectively (compare to curves for 4.5 μJ in figure 5).

6. Summary and conclusion

In this contribution we investigated via spectral interferometry the early time dynamics of free-electron plasma produced in a thin water jet after excitation with temporally shaped ultrashort laser pulses. Assuming homogeneous excitation—being valid in the low excitation regime—free-electron density is directly proportional to the phase shift observed in the spectral interference between a reference pulse propagating before the pump and a probe pulse propagating after it. Making use of common-path techniques allowed us to develop an ultrastable set-up that enlarged the temporal measurement window into several ps regime without the need for a high-resolution spectrometer.

With respect to temporally asymmetric shaped laser pulses we observed that positive TOD shaped pulses create a much higher free-electron density than their time-reversed counterparts. The reason for this behavior is the interplay between the two ionization mechanisms, i.e. multiphoton ionization and avalanche ionization.

A simple rate equation model confirmed that avalanche ionization starting from free electrons created by photoionization has a much higher contribution for pulses shaped with positive TOD than for negative ones. Taking electron densities created by the bandwidth-limited pulse into account we derived a value for the multiphoton coefficient. We then adjusted the avalanche coefficient to the electron densities resulting from excitation with positive TOD shaped pulses. Then, we calculated electron densities for the negative TOD pulses keeping the coefficients fixed and found good agreement with the measured ones. We therefore believe that our approach based on temporally shaped laser pulses helps to determine multiphoton and avalanche coefficients in a more reliable way than was hitherto possible. Moreover, we have shown directly that temporally shaped laser pulses can be used to control basic ionization processes in dielectrics. As this is the first step in optical break down that together with propagation effects and ultrafast phase changes eventually leads to laser processing of high band gap transparent materials, this might also be relevant to controlled high precision material processing. Note within that context that structures down to the 100 nm scale in the far field of a microscope objective have been created with temporally shaped pulses [9, 34]. In general, optimal energy coupling with the help of suitably shaped temporal pulse envelopes opens the route to guiding the material response toward user-designed directions [35].

Acknowledgment

Financial support by the Deutsche Forschungsgemeinschaft DFG within the priority program 1327 is gratefully acknowledged.

References

[1] Sugioka K, Meunier M and Piqué A (ed) 2010 *Laser Precision Microfabrication* (Berlin: Springer)
[2] Phipps R (ed) 2010 *International Symposium on High Power Laser Ablation* (Melville, NY: AIP)
[3] Vogel A and Venugopalan V 2003 *Chem. Rev.* **103** 577
[4] Vogel A, Noack J, Hüttman G and Paltauf G 2005 *Appl. Phys.* B **81** 1015

[5] Keldysh L V 1965 *Sov. Phys.—JETP* **20** 1307
[6] Noack J and Vogel A 1999 *IEEE J. Quantum Electron.* **35** 1156
[7] Rethfeld B 2006 *Phys. Rev.* B **73** 035101
[8] Feit M D, Komashko A M and Rubenchik A M 2004 *Appl. Phys.* A **79** 1657
[9] Englert L, Rethfeld B, Haag L, Wollenhaupt M, Sarpe-Tudoran C and Baumert T 2007 *Opt. Express* **15** 17855
[10] Sacchi C A 1991 *J. Opt. Soc. Am.* B **8** 337
[11] Assion A, Wollenhaupt M, Haag L, Mayorov F, Sarpe-Tudoran C, Winter M, Kutschera U and Baumert T 2003 *Appl. Phys.* B **77** 391
[12] Mao X, Mao S S and Russo R E 2003 *Appl. Phys. Lett.* **82** 697
[13] Abraham E, Minoshima K and Matsumoto H 2000 *Opt. Commun.* **176** 441
[14] Gawelda W, Puerto D, Siegel J, Ferrer A, Ruiz de la Cruz A, Fernandez H and Solis J 2008 *Appl. Phys. Lett.* **93** 121109
[15] Mao S S, Quéré F, Guizard S, Mao X, Russo R E, Petite G and Martin P 2004 *Appl. Phys.* A **79** 1695
[16] Sarpe-Tudoran C, Assion A, Wollenhaupt M, Winter M and Baumert T 2006 *Appl. Phys. Lett.* **88** 261109
[17] Temnov V V, Sokolowski-Tinten K, Zhou P and von der Linde D 2004 *Appl. Phys.* A **78** 483
[18] Temnov V V, Sokolowski-Tinten K, Zhou P, El-Khamhawy A and von der Linde D 2006 *Phys. Rev. Lett.* **97** 237403
[19] Tokunaga E, Terasaki A and Kobayashi T 1992 *Opt. Lett.* **17** 1131
[20] Martin P, Guizard S, Daguzan P, Petite G, d'Oliveira P, Meynadier P and Perdrix M 1997 *Phys. Rev.* B **55** 5799
[21] Audebert P *et al* 1994 *Phys. Rev. Lett.* **73** 1990
[22] Quéré F, Guizard S and Martin P 2001 *Europhys. Lett.* **56** 138
[23] van Dijk M A, Lippitz M, Stolwijk D and Orrit M 2007 *Opt. Express* **15** 2273
[24] Wollenhaupt M, Krug M, Köhler J, Bayer T, Sarpe-Tudoran C and Baumert T 2009 *Appl. Phys.* B **95** 245
[25] Köhler J, Wollenhaupt M, Bayer T, Sarpe C and Baumert T 2011 *Opt. Express* **19** 11638
[26] Wollenhaupt M *et al* 2002 *Phys. Rev. Lett.* **89** 173001
[27] Born M and Wolf E 1999 *Principles of Optics* (Cambridge: Cambridge University Press)
[28] Christensen B H and Balling P 2009 *Phys. Rev.* B **79** 155424
[29] Wollenhaupt M, Englert L, Horn A and Baumert T 2010 *Proc. SPIE* **7600** 76000X-1
[30] Wollenhaupt M, Assion A and Baumert T 2007 *Springer Handbook of Lasers and Optics* (New York: Springer) chapter 12
[31] Stuart B C, Feit M D, Herman S, Rubenchik A M, Shore B W and Perry M D 1996 *Phys. Rev.* B **53** 1749
[32] Kennedy P K 1995 *IEEE J. Quantum Electron.* **31** 2241
[33] Fan C H, Sun J and Longtin J P 2002 *J. Appl. Phys.* **91** 2530
[34] Englert *et al* 2012 *J. Laser Appl.* at press
[35] Stoian R, Wollenhaupt M, Baumert T and Hertel V 2010 *Springer Series in Materials Science* vol 135 (Berlin/Heidelberg: Springer) chapter 5